ACS SENSORS

pubs.acs.org/acssensors

Article

Photothermal-Reagent-Triggered Visual Thermoresponsive and Quantized Photoelectrochemical Dual-Signal Assay

Lin Li, Hongmei Yang, Li Li,* Xiaoran Tan, Shenguang Ge, Lina Zhang, Jinghua Yu,* and Yan Zhang*

Cite This: *ACS Sens.* 2022, 7, 2429−2437

Read Online

ACCESS | Metrics & More | Article Recommendations | Supporting Information

ABSTRACT: In vitro biosensing chips are urgently needed for early-stage diagnosis and real-time surveillance of epidemic diseases. Herein, a versatile zone with photothermal effects is implanted in the miniature space of a collapsible lab-on-paper photoelectrochemical biosensor for on-site detection of microRNA-141 in body fluids, which can flexibly interconnect the traditional photocurrent signal with functional temperature response. The visualized thermoresponsive results are enhanced by the exciton energy conversion between Fe_3O_4 nanoparticles (Fe_3O_4 NPs) and formed Prussian blue nanoparticles under near-infrared irradiation, which not only presents heat energy gradient variations but also generates color changes. Significantly, the controlled release of Fe_3O_4 NPs is actuated by a target-triggered enzyme assist strand displacement cycle strategy to efficiently improve the accuracy of target temperature signal prediction, which can concurrently mediate photoelectric signal attenuation via promoting the rapid recombination of photoexcited charge carriers on the $CuInS_2/CoIn_2S_4$ electrode surface, affording dependable ultrasensitive detection results. Benefitting from the ingenious design of the versatile thermoresponsive-photoelectric sensing platform, the preliminary screening and ultrasensitive quantitative analysis can be simultaneously achieved in a single-drop sample. As a consequence, speedy prediction results and satisfied monitoring data are acquired in the ranges of 0.5 pM to 2 nM and 0.001 pM to 5 nM by measuring the temperature change and photocurrent intensity. By right of these advantages, such research paves a prospective paradigm for the manufacture of a visual, rapid, broad-spectrum, and reliable real-time surveillance platform, which allows it to be a promising candidate for epidemic disease home diagnosis and intelligent diagnosis.

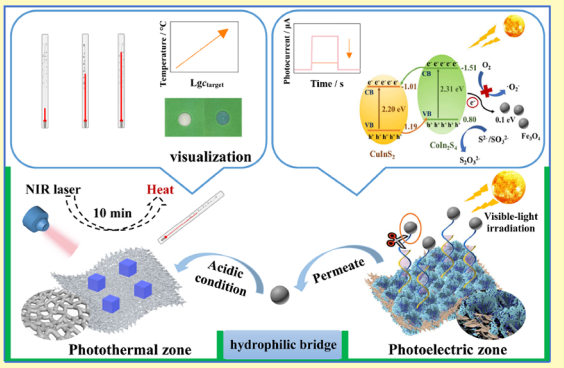

KEYWORDS: *photoelectrochemical, photothermal, lab-on-paper, dual-signal, microRNA*

Over the recent period, paper-based flexible sensors have been widely used in the point-of-care testing (POCT) field; they are expected to become a greatly promising candidate tool for in vitro detection.[1,2] Its popularity lies in the inherent advantages of inexpensiveness, rapidness, light weight, and user-friendliness, especially suitable in family disease diagnosis.[3,4] In addition, the integratable origami-chip platform makes it possible to the migration of a functional biological matrix at the surface by intrinsic hydrophilic fluidic pathways, thus ensuring efficient interworking of the zones.[5] Currently, various techniques such as fluorescence,[6] chemiluminescence,[7] and electrochemistry[8] have been introduced into the origami chip for clinical monitoring and quantitative screening in the POCT field. Although a tremendous practical utility has been demonstrated, several limitations still exist in on-site detection, including the expensive and complicated diagnosis with detection procedures.[9,10] Hence, fabricating a rapid, simple, and reliable POCT system for biomarker monitoring induced a huge significance on the home diagnosis and intelligent diagnosis.

Unfortunately, the deviation of visual discrimination caused by color gradient or depth changes, relatively poorer sensitivity, and lower clinical assay accuracy are inevitable in the current primary semi-quantitative POCT tools with yes/no-type results,[11,12] leading to an unguaranteed stability of monitoring results. Temperature-based measurements use photothermal-responsive materials as "nanoreactors" to establish a bridge connecting photon energy, heat energy, and analytes in the physiological matrix,[13−15] which has good anti-interference performance.[16,17] Particularly, with the aid of handheld devices, the photothermal nanoreactors are driven to produce visible and determinable heat readings, which require neither cumbersome instruments nor the subjective impressions of unaided-eye observation.[18] The potential practicability of the photothermal sensor in the POCT system also increases the integratability and deliverability of the analytical device.

Received: May 31, 2022
Accepted: July 25, 2022
Published: August 5, 2022

https://doi.org/10.1021/acssensors.2c01162
ACS Sens. 2022, 7, 2429−2437

However, the thermosensitive sensing strategy has to be compromised in sensitivity and spatiotemporal controllability of the trace analyte detection method.

Recently, the lab-on-paper photoelectrochemical (PEC) bioanalysis devices utilize semiconductor materials as photo-energy-transducing elements and specific nucleic acids as signal identification modules, which have blossomed into one of the ideal ultrasensitive POCT platforms benefiting from the fast response, effortless manipulation, and high sensitivity.[19−21] The photoelectric unit with a sensitized structure is an indispensable part for PEC to ameliorate the utilization rate of photon energy and accelerate the charge conversion of the internal electric field.[22,23] Copper indium disulfide ($CuInS_2$) as a new ternary sulfide with low toxicity, multiple electroactive centers, and high conductivity[24,25] has been broadly employed in photoelectric devices[26] and photocatalysis[27,28] for enhancing system performance. However, the individual materials have poor photoelectroactivity, mainly derived from the frequent charge carrier recombination. Hence, the granular cobalt indium tetrasulfide ($CoIn_2S_4$) is introduced as a hole capture center to restrict interlayer recombination of photogenerated carriers,[29,30] and the charge density of the rock-bottom optical energy interface element can also be observably enhanced. Subsequently, the functional DNA as the target-biometric sequence is anchored on the surface of the photosensitive unit, which is endowed with photoelectric signal variation via stepwise assembly to realize a conversion rate of 1:N (N > 1) signal.[31,32] While it reveals outstanding sensitivity and specificity, the classical optoelectronic switch technique only responding single−signal is susceptible to latent influences from the complex bioassay matrix, which restricts applications for regular home monitoring in at-risk individuals. Therefore, taking advantages of miniaturization and multifunction integrability in the lab-on-paper, the photothermal sensor is introduced into the microfluidic PEC device for POCT, which compensates their limitation in a synergistic fashion and provides a new method for expanding a type of analysis platform with dual-signal and universal capability.[33,34]

Herein, a thermoresponsive-photoelectric sensing platform is constructed by integrating spatially separable photothermal agents (PTAs) as a light-to-heat energy transducer and $CuInS_2/CoIn_2S_4$ as a photoelectric converter in foldable lab-on-paper for on-site detection of microRNA-141, which generates dosage-dependent thermal/photoelectric signal variation (Scheme 1). Specifically, the Fe_3O_4 nanoparticles (Fe_3O_4 NPs) are released with control by a target-triggered enzyme assist strand displacement cycle strategy to compete for shunting the photoinduced carrier and inhibiting electron transfer in the photoelectric zone. Meanwhile, a hydrophilic bridge with fluid instantaneous movement functions can transfer Fe_3O_4 NPs to the photothermal zone in the lab-on-paper, which contains an acidic material that converts Fe_3O_4 NPs into Prussian blue nanoparticles (PB NPs) with photothermal properties and a special color. Subsequently, under the near-infrared (NIR)/visible light irradiation, the temperature begins to fluctuate with photoelectric signal recovery, realizing the dual-signal output. The established thermoresponsive-photoelectric sensing platform offers a speedy, broad-spectrum, and reliable thermometric warning method in real systems through a handheld laser device, which provides a favorable early-stage diagnosis tool to promote early medical intervention and immediate home surveillance.

Scheme 1. Schematic Illustration of a Lab-on-Paper Thermoresponsive-Photoelectric Sensor

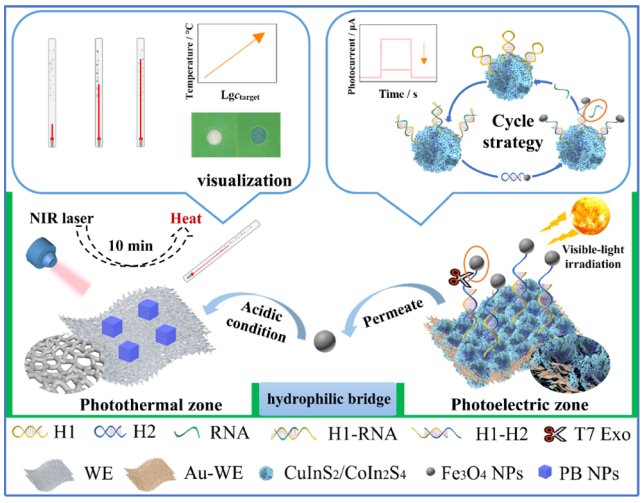

EXPERIMENTAL SECTION

Preparation of the Thermoresponsive-Photoelectric Sensing Chip. Prior to fabrication, the layout of thermoresponsive-photoelectric sensing chip was designed with three particular functional units for sample injection, reagent storage, and signal detection, as illustrated in Figure S1. After printing on chromatographic paper using the solid wax printing technology, the fabricated wax patterns were obtained and transferred to a hot plate to construct hydrophobic walls. Then, the shaded area at the edge of the sample injection pad and the signal detection pad were trimmed to hollow parts. It could be seen that each unit contained two signal output areas named photoelectric zone I and photothermal zone II. In detail, the sample injection pad consisted of two hollowed white parts defined as the reagent inlet and signal outlet and a hydrophilic channel for controlling transfer of PTAs in the dual zone, facilitating sensitive detection of temperature variation to realize the result prejudge. The reagent storage pad was provided with a semi-hydrophobicity and semihydrophilicity layer in zone I containing a Ag/AgCl reference electrode and a carbon counter electrode to ensure the connectivity of current transfer during the photoelectric testing, while adjacent zone II was used as a hydrophobic reservoir to prevent penetration of photothermal reagents (Figure S1a). A unique hydrophilicity dual channel (gray) was created in the signal detection pad, in which the seed-mediated growth technique was used to assist the formation of Au nanoparticles (Au NPs) to obtain a working electrode (Au-WE) with an efficient electrofluidic structure in zone I. Notably, the Au-WE also had a natural photothermal effect in the NIR laser-driven process, which seriously interferes with the accuracy of the temperature signal in the detection process. Therefore, the thermoresponsive-photoelectric sensing platform was designed as a dual-zone layout to eliminate intervention of working electrodes. Ultimately, the lab-on-paper was folded to expose three screen-printed electrodes and connected with an electrochemical workstation to accomplish accurate collection of photoelectric signals (Figure S1b).

Assembly of the $CuInS_2/CoIn_2S_4$ Heterojunction. Primitively, an Au NP layer was functionalized on the nanoscale fibers in zone I of the signal detection pad for enlarging the surface-to-volume ratio and electric conductivity. Next, the petaloid $CuInS_2/CoIn_2S_4$ was grown on Au-WE by the one-pot hydrothermal method under optimal conditions (details shown in the Supporting Information). During the synthesis procedure, 0.0640 g of $CoCl_2{\cdot}6H_2O$, 0.0306 g of $CuCl{\cdot}2H_2O$, 0.1022 g of $InCl_3{\cdot}4H_2O$, and 0.3405 g of $C_6H_8O_7$ were first dissolved in 35 mL of deionized water; then 0.1083 g of thioacetamide was added and stirred in ambient surroundings for 5 min. Subsequently, the mixture was transferred to a Teflon autoclave with Au-WE suspended on the surface of the solution and placed at 120 °C for 5 h to provide an appropriate growth circumstance. After

https://doi.org/10.1021/acssensors.2c01162
ACS Sens. 2022, 7, 2429−2437

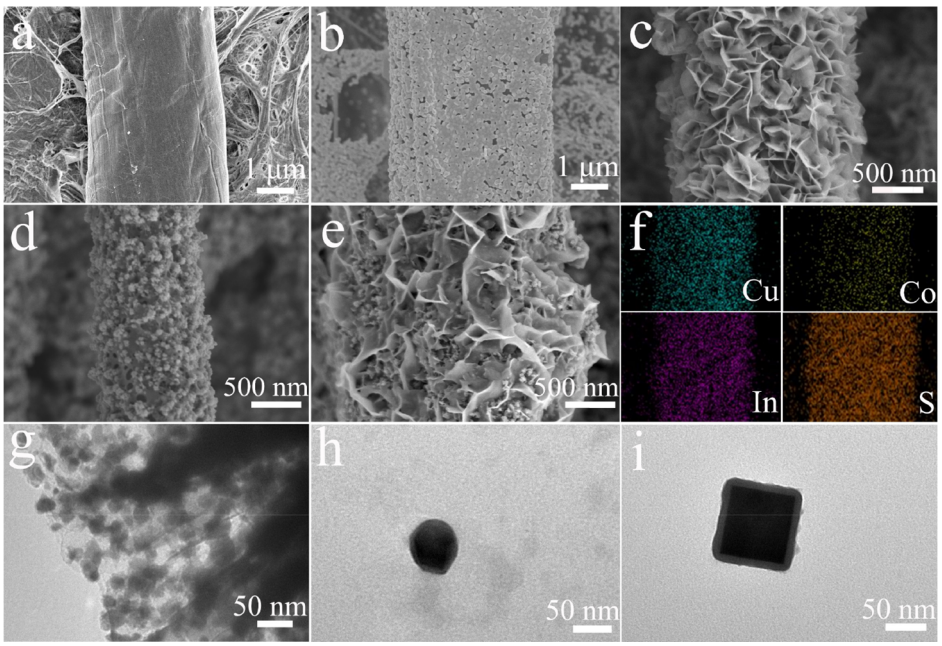

Figure 1. SEM images of (a) bare paper fibers, (b) Au-WE, (c) $CuInS_2$/Au-WE, (d) $CoIn_2S_4$/Au-WE, and (e) $CuInS_2$/$CoIn_2S_4$/Au-WE. (f) Elemental mapping analysis of $CuInS_2$/$CoIn_2S_4$/Au-WE. TEM images of (g) $CuInS_2$/$CoIn_2S_4$, (h) hairpin DNA-modified Fe_3O_4 NPs, and (i) PB NPs.

completing these steps, the lab-on-paper was washed with water and dried overnight at 60 °C and the ideal $CuInS_2$/$CoIn_2S_4$ heterojunction was obtained on Au-WE.

Thermoresponsive-Photoelectric Sensing Analysis. Typically, 20 μL of (3-aminopropyl)triethoxysilane (2 wt %) and 20 μL of glutaraldehyde (2.5 wt %) were dropped onto the surface of $CuInS_2$/$CoIn_2S_4$/Au-WE in order to immobilize hairpin DNA (H1, specific nucleic acid sequences are shown in Table S1) via aldimine condensation reaction.[35] Next, 20 μL of H1 (5 μM) was applied on the electrode surface and incubated at 37 °C for 2 h; then the nonspecific adsorption sites were blocked by 1 mM monoethanolamine, followed by addition of the miRNA-141 solution and incubation at 37 °C for 1 h to open hairpin H1. Subsequently, 10 μL of H2−Fe_3O_4 NPs (5 μM) and H1−miRNA-141 were mixed, and the reaction mixture was heated to 37 °C for 2 h to generate H1−H2−Fe_3O_4 NPs. Meanwhile, miRNA-141 were released to continue combining with unopened hairpin H1. Later, a penetratively longitudinal path could be formed by folding reagent storage pads and signal detection pads to obtain the preliminary signal. Following this, 10 μL of T7 exonuclease (T7 Exo) was incubated in the mixture at 25 °C for 3 h, which could degrade the H1−H2−Fe_3O_4 NP hybrid strand structure and loosen the Fe_3O_4 NPs. For collecting the photothermal signal, the lab-on-paper was folded in order as shown in Figure S1b. Then the free Fe_3O_4 NPs were allowed to flow to zone II of the signal detection pad through capillary action of hydrophilic channels of the sample injection pad and react with pre-embedded HCl (0.1 M) and $K_4Fe(CN)_6{\cdot}3H_2O$ (90 mM) to prepare PB NPs. Thirty minutes later, the PB NPs were irradiated with NIR (808 nm, 3 W cm^{-2}) light for 300 s, and the predictive signal was recorded using a handheld infrared thermometer. Finally, three printed electrodes were linked with the electrochemical workstation to record the photocurrent signal by applying a 300 W Xe lamp at 0.0 V (vs Ag/AgCl) potential.

RESULTS AND DISCUSSION

Working Principle. The thermoresponsive-photoelectric microfluidic sensing platform was realized through the enzyme assist strand displacement cycle strategy to generate photoelectric signal attenuation and target dosage-dependent heat enhancement under the visible light/NIR irradiation, as shown in Scheme S1. Primarily, H1 was assembled on the photoelectroactive site surface in zone I via aldimine condensation reaction.[37] When the target existed (using miRNA-141 as a model), the hairpin DNA was untied and annealed to form the heteroduplex (H1−miRNA-141) with complementary bases. Afterward, the introduction of H2−Fe_3O_4 NPs initiated the SDR reaction; the binding energy between H2−Fe_3O_4 NPs and exposed H1 was activated, leading to the formation of hybrid chains and the release of intact miRNA-141. The target was reused, and the exponential H1−H2−Fe_3O_4 NP hybrid chains were outputted for competitive shunt electron, which effectively inhibited electron transfer, resulting in photoelectric signal reduction. Subsequently, the Fe_3O_4 NPs were freed by adding T7 Exo, which was transferred to the zone II via fluid instantaneous movement in the hydrophilic channel. The Fe_3O_4 NPs were transformed into PB NPs under acidic conditions to form a thermosensitive element with NIR irradiation. Meanwhile, H1 was reverted to start the next cycle. Particularly, driven by NIR light, the photon energy interacts effectively with the PB NP lattice, increasing lattice vibration and converting photon energy into stronger thermal effects.[36] Ultimately, the bridge between the photocurrent signal and temperature signal was established under the trigger of the target, constituting a dual-signal detection mode.

Material Characterization. The morphology features of the signal detection pad in zone I (Figure S1) after layer-by-layer modification were studied by scanning electron microscopy (SEM) and transmission electron microscopy (TEM). Compared with the bare fibers (Figure 1a), the Au NP structures with a mean diameter of about 50 nm were uniformly distributed over paper fibers to form the working electrode (Au-WE), which could effectively promote electron transfer in interfaces and electrical conductivity (Figure 1b). On this basis, $CuInS_2$/$CoIn_2S_4$/Au-WE (Figure 1e,g) was prepared by the surface in situ growth method, which was

https://doi.org/10.1021/acssensors.2c01162
ACS Sens. 2022, 7, 2429−2437

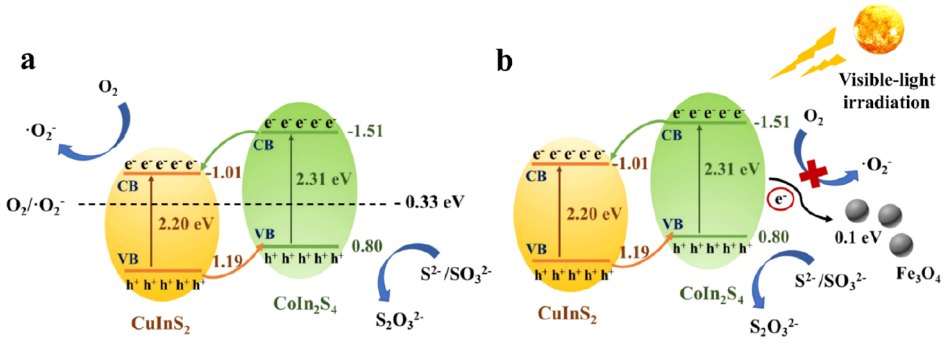

Figure 2. (a) $CuInS_2/CoIn_2S_4$ charge-carrier transfer and (b) Fe_3O_4 NPs inhibit mechanisms on photoelectric zone I.

mainly composed of petaloid $CuInS_2$ flakes (Figure 1c) and covered with equably dense $CoIn_2S_4$ particles (30−50 nm diameter, Figure 1d). These rougher surfaces not only increased the specific surface area of photoelectric response to incorporate a mass of photon energy but also facilitated binding with hairpin DNA. Identically, energy-dispersive X-ray spectrometry element mapping further revealed the uniform distribution of Au, C, Cu, Co, In, and S elements on the electrode surface, as demonstrated in Figures 1f and S4a,b. The morphological changes of photothermal particles in zone II were investigated by TEM images. Specifically, the spherical NPs (Figure 1h) gradually disappeared with the appearance of increasingly clear cubic structures (Figure 1i), confirming the successful preparation of PB NPs.[36]

Furthermore, X-ray photoelectron spectroscopy (XPS) was utilized to verify the surface chemical state and detail element valence composition of $CuInS_2/CoIn_2S_4$/Au-WE. In addition to the presence of Cu, In, and S elements in the heterojunction, a peak was detected in the wide scan spectrum, belonging to Au-WE, as illustrated in Figure S2a. Concretely, two obvious peaks at 88.2 and 84.5 eV belonging to Au $4f_{5/2}$ and Au $4f_{7/2}$, respectively, were induced by Au NPs (Figure S2b). The unambiguous peaks of the Cu 2p spectrum were ascribed to Cu $2p_{3/2}$ (931.8 eV) and Cu $2p_{1/2}$ (951.7 eV) originating from Cu^+ (Figure S2c). From the Co 2p spectrum, it was observed that the peak values near 778.9 eV corresponded to Co $2p_{3/2}$ and peaks near 794.1 eV corresponded to Co $2p_{1/2}$, demonstrating that the chemical valence of Co in the heterostructure was +2 (Figure S2d). Furthermore, the prominent peaks of the In element located at 444.9 and 452.5 eV (Figure S2e) were consistent with In $3d_{5/2}$ and In $3d_{3/2}$, respectively, while the characteristic peaks at 161.7 and 162.8 eV (Figure S2f) were in accordance with S $2p_{3/2}$, and S $2p_{1/2}$, respectively. Moreover, X-ray diffraction (XRD) patterns were analyzed to further characterize the crystalline structure and purities of $CuInS_2/CoIn_2S_4$/Au-WE. The distinct characteristic peaks of the petaloid $CuInS_2$ belonged to (002), (101), (112), (200), (213), (220), (215), (224), and (316) crystal planes, matching well with the standard JCPDS card no. 38-0777 (orange curve, Figure S2g).[37] The broad peaks of the granular $CoIn_2S_4$ were consistent with JCPDS card no. 79-1015,[30] which were attributed to (111), (220), (311), (400), (511), (440), (642), and (840) diffraction surfaces, respectively (green curve, Figure S2g). Apparently, the XRD pattern of the $CuInS_2/CoIn_2S_4$ heterojunction corresponded to that of pure $CuInS_2$ and $CoIn_2S_4$ crystal planes, confirming that $CuInS_2$ and $CoIn_2S_4$ existed in the heterojunction as a skeleton structure (red curve, Figure S2g). Besides, the Au-WE was further verified by XRD analysis (Figure S4d). Except that the diffraction peak of the (002) crystal plane was consistent with cellulose (JCPDS card no. 03-0289),[38] another four apparent peaks were detected in the XRD pattern, which were well indexed to the (111), (200), (220), and (311) planes of Au NPs (JCPDS card no. 04-0784).[39] Especially, the Au-WE peaks were not observed in the XRD pattern of $CuInS_2/CoIn_2S_4$/Au-WE, mainly because the peaks of $CuInS_2/CoIn_2S_4$ overlap a lot with Au-WE. In summary, these crystal characteristics were consistent with the XPS results, which preliminarily certified that the heterostructure on the Au-WE surface incorporated $CuInS_2$ and $CoIn_2S_4$.

Evaluation of the Photoinduced Electron Generation Property and Mechanism. The semiconducting property was profiled by the UV−vis spectrum, Tauc plots, Mott−Schottky (M−S) curves, and steady-state photoluminescence (PL) spectra. As presented in Figure S2h, the absorption edges of $CuInS_2$/Au-WE and $CoIn_2S_4$/Au-WE existed at approximately 430 and 450 nm, respectively. In contrast, $CuInS_2/CoIn_2S_4$/Au-WE exhibited higher optical absorption intensity at visible light ranging from 500 to 800 nm, which contributed to accumulation of photons on the heterojunction and further enhancement of efficient charge transfer in the visible-light-driven process. Then, the Tauc plots were constructed according to Kubelka−Munk theorem, with the corresponding band gap energies (E_g) of $CuInS_2$/Au-WE and $CoIn_2S_4$/Au-WE found to be at 2.20 and 2.31 eV, respectively (Figure S2i). Subsequently, the band-edge positions and semiconductor types of $CuInS_2$/Au-WE and $CoIn_2S_4$/Au-WE were measured by M−S curves in the three-electrode system (Figure S2j,k). Obviously, the positive slope of the curves suggested that $CuInS_2$ and $CoIn_2S_4$ were n-type semiconductors[40] with flat-band potentials (V_{fb}) of −0.81 and −1.31 V (vs Ag/AgCl, pH 6.70), respectively.[41,42] Meanwhile, the E_{CB}/E_{VB} of $CuInS_2/Au$-WE and $CoIn_2S_4$/Au-WE were calculated as −1.01/1.19 and −1.51/0.80 V, respectively. The above results proved that a valid heterostructure was formed and well consistent with the photocurrent density result. In addition, the PL spectra were utilized for in-depth research charge recombination behavior of the semiconductor by photoinduction. All the PL emission peaks of $CuInS_2/CoIn_2S_4$/Au-WE, $CuInS_2$/Au-WE, and $CoIn_2S_4$/Au-WE were located at about 560 nm (the excitation wavelength was 375 nm), as shown in Figure S2l. Remarkably, the PL emission intensity of $CuInS_2/CoIn_2S_4$/Au-WE was lower than that of pure $CuInS_2$/Au-WE and $CoIn_2S_4$/Au-WE, revealing that the separation efficiency of photoexcited e^-/h^+ pairs was improved.

The schematic explanation of correlative precise E_g levels and the photoexcited charge-carrier separation mechanism in

https://doi.org/10.1021/acssensors.2c01162
ACS Sens. 2022, 7, 2429−2437

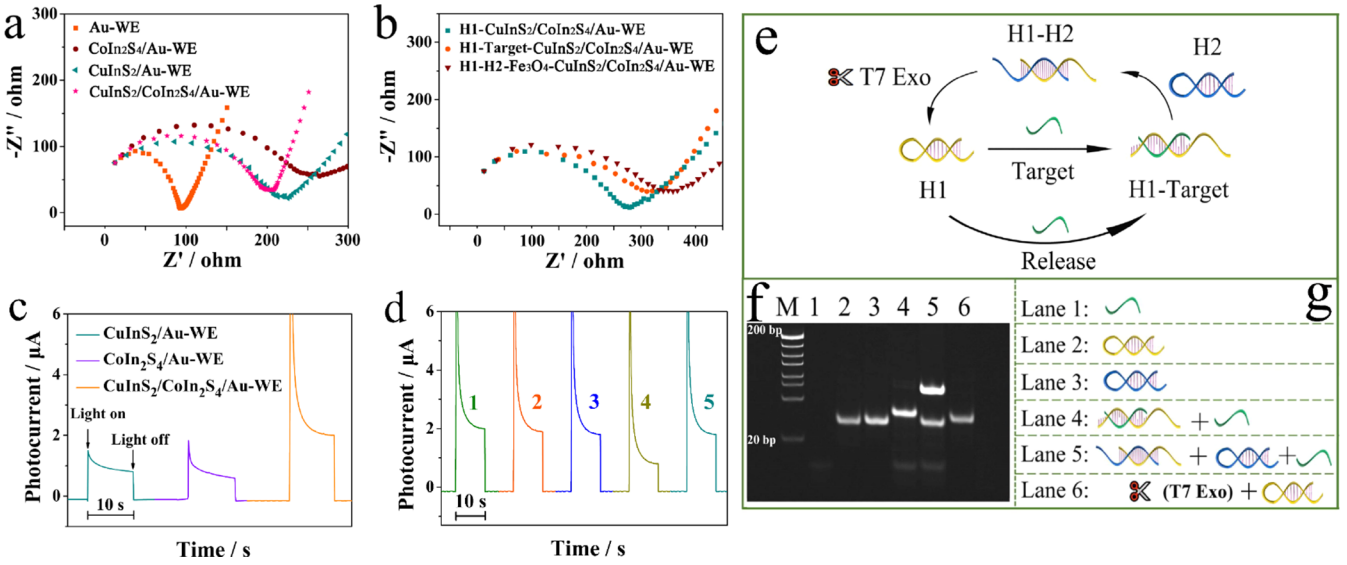

Figure 3. (a–c) EIS plots and photocurrent response curves of different samples. (d) PEC responses of $CuInS_2/CoIn_2S_4$/Au-WE (1), H1–$CuInS_2/CoIn_2S_4$/Au-WE (2), H1-Target–$CuInS_2/CoIn_2S_4$/Au-WE (3), H1–H2–Fe_3O_4 NPs–$CuInS_2/CoIn_2S_4$/Au-WE (4), and cutting H1–H2–Fe_3O_4 NPs–$CuInS_2/CoIn_2S_4$/Au-WE with T7 Exo (5). (e) Mechanism of the cyclic amplification strategy. (f) PAGE characterization and (g) diagram of cyclic reaction products.

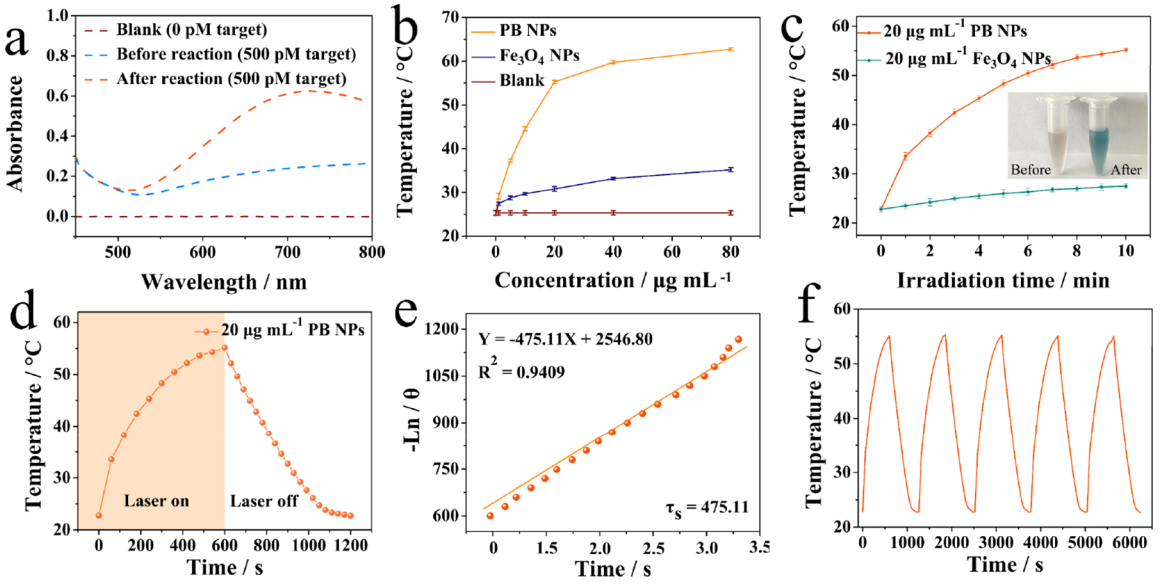

Figure 4. (a) UV–vis spectra of the hairpin DNA modified by PTAs before and after the irradiation. (b,c) Effects of PTA concentration and laser irradiation time on temperature (insets: color contrast before and after the irradiation). (d) Photothermal effect of PTAs (20 μg mL^{-1}) irradiated by 808 nm laser for 600 s and shutting off to natural cooling. (e) Negative natural logarithm ($-\mathrm{Ln}\ \theta^{-1}$) of the driving force temperature vs the linear time data from the cooling period is used to determine τ_s. (f) Photothermal conversion cycling test of PTAs (20 μg mL^{-1}) under 808 nm laser (3 W cm^{-2}).

the heterojunction is illustrated in Figure 2a. Under visible light, the electrons of bare $CuInS_2$ or $CoIn_2S_4$ were photoinduced to the conduction band (CB), while the valance band (VB) extracted photogenerated holes. However, e^-/h^+ pairs formed by competition can be promptly recombined, resulting in weak photoelectric activity. Noteworthily, the formation of the $CuInS_2/CoIn_2S_4$ heterostructure effectively promoted the multiplication of the background photocurrent signal since a large number of photoinduced electrons from the CB of the $CoIn_2S_4$ layer concentrated on that of the $CuInS_2$ layer, while the photoinduced holes were rapidly extracted from the VB of the $CuInS_2$ layer to that of the $CoIn_2S_4$ layer, as shown in Figure 2a. Obviously, the CB level of the $CuInS_2$ layer was significantly higher than the redox potential of O_2/O_2^- (−0.33 eV vs NHE), which was identical to the outcome of radical species capturing. Then the recombination of e^-/h^+ pairs was effectively suppressed and provided enriched photoelectroactive sites. Nonetheless, when the Fe_3O_4 NPs were formed on the electrode surface, its CB layer was involved in partial electron aggregation, resulting in that electron failed to be transmitted to the $CuInS_2$. Simultaneously, the h^+ in the VB layer were rapidly recombined with the e^- in the electrolyte due to a narrow E_g (0.1 eV), leading to a severely attenuated signal (Figure 2b).

https://doi.org/10.1021/acssensors.2c01162
ACS Sens. 2022, 7, 2429–2437

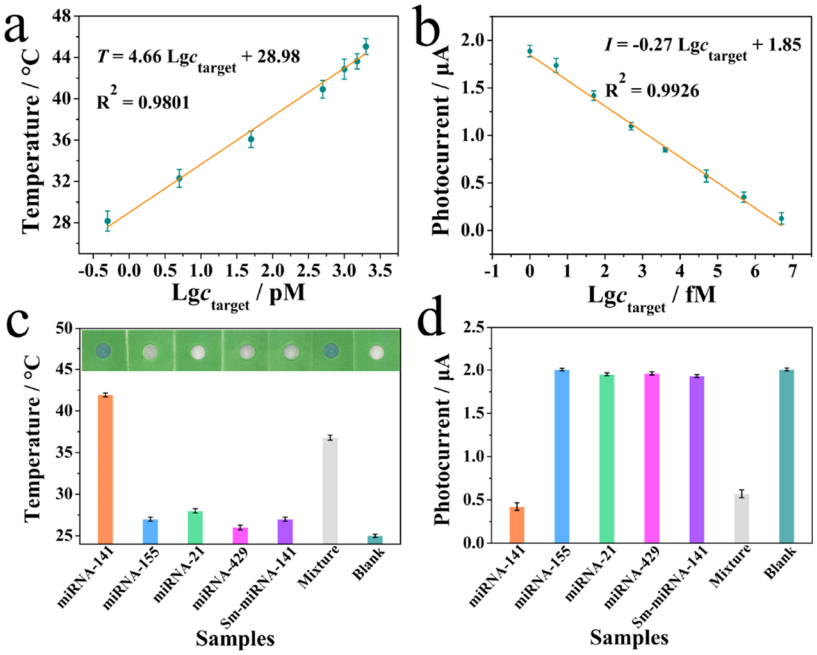

Figure 5. (a) Calibration curves of the temperature signals toward different concentrations of miRNA-141 (0.5, 5, 50, 5×10^2, 10^3, 1.5×10^3, 2×10^3 pM) and (b) photoelectric signals with different concentrations of miRNA-141 (1, 5, 50, 5×10^2, 4×10^3, 5×10^4, 5×10^5, 5×10^6 fM). (c,d) Selectivity investigation of the thermoresponsive-photoelectric sensing platform (insets: photographs of the colorimetric sample selectivity investigation).

Feasibility Study of the Thermoresponsive-Photoelectric Sensing Platform. Electrochemical impedance spectroscopy (EIS) and photocurrent−time curves were used to explain the effect of the modified sensor interface on separation and charge transfer. Specifically, the Nyquist plots of different electrodes illustrated different semicircle curves in the sequence of Au-WE < $CuInS_2/CoIn_2S_4$/Au-WE < $CuInS_2$/Au-WE < $CoIn_2S_4$/Au-WE (Figure 3a), indicating that the construction of the $CuInS_2/CoIn_2S_4$ heterojunction inhibited the recombination of e^-/h^+ pairs. With stepwise assembling of H1, miRNA-141, and H2−Fe_3O_4 NPs, the electron-transfer resistance (R_{et}) successively increased (Figure 3b), which suggested that the formation of the hybridization chain enhanced electrostatic repulsion with reduced conductivity. Undeniably, all results were in accordance with the photocurrent density (Figure 3c,d). Especially, after Fe_3O_4 NP dissociation, the recombination of e^-/h^+ pairs on the electrode surface was again restrained, and the photocurrent produced gradually increased (Figure 3(d-4)). The aforementioned results manifested that the photoenergy-transducing elements were successfully constructed.

Moreover, to verify the practicability of the enzyme-assisted strand displacement cycle amplification strategy, 15% polyacrylamide gel electrophoresis (PAGE) analysis was carried out (Figure 3e). Distinctly, the H1−miRNA-141 (lane 4) and H1−H2 (lane 5) hybrid duplexes appeared after finishing the SDR reaction compared to the single-strand miRNA-141 (lane 1), H1 (lane 2), and H2 (lane 3), as described in Figure 3f,g. When T7 Exo existed in the system, the hybrid duplex bands disappeared (lane 6). Unsurprisingly, the extra bands in lanes 4, 5, and 6 were reaction products of a cyclic strategy, including single-stranded DNA and targets. The aforementioned PAGE results evidently certified the successful preparation of the cyclic amplification strategy in response to miRNA-141.

Evaluation of the Photothermal Property. To certify the feasibility of the thermosensitively responsive materials as the photothermal detecting element on the thermoresponsive-photoelectric microfluidic platform, UV−vis spectroscopy was determined to first prove the optical absorption properties of PTAs (Figure 4a). The results displayed that the PB NPs could be regarded as a temperature-detecting component in the biosensor device without interference from other solvents in the NIR scope. This phenomenon was initiated by the absorption photons in the exciton-transfer transition between Fe(II) and Fe(III), which constituted the electronically excited state with excess energy. The superfluous photon energy then drops from the excited state, eventually causing the energy transition from photon to heat energy. Therefore, 808 nm NIR laser was introduced into the photothermal zone II for the following experiments. Then, the properties of PTAs were investigated, including PB NPs, Fe_3O_4 NPs, and the blank. Preliminarily, the exfoliated PTAs were exposed in different solutions for reaction and irradiated with 808 nm NIR laser for 10 min. Under the action of PB NPs, the temperature of the system gradually reached as high as 65 °C, with an increase in the concentration of thermosensitively responsive materials (Figure 4b). However, the temperature of other materials increased much less than that. At the same concentration (20 $\mu g\ mL^{-1}$), a hand-held thermometer was used to measure the temperature every 1 min. The results were consistent with that mentioned above and accompanied by a transition from a transparent color to a typical blue color (Figure 4c). The photothermal conversion efficiency was 8.53%, calculated by the previously reported method (Figure 4d,e).[43] Moreover, the PTAs showed outstanding photothermal stability after five cycles of laser irradiation (Figure 4f), indicating the great superiority of the PB NPs on the thermoresponsive-photoelectric microfluidic platform.

https://doi.org/10.1021/acssensors.2c01162
ACS Sens. 2022, 7, 2429−2437

Analytical Performance. Under optimized experimental circumstances (details can be found in the Supporting Information and Figure S5), the sensitivity and quantitative capacity of the presented thermoresponsive-photoelectric sensing platform were assessed via incubating with various concentrations of miRNA-141. It could be obviously seen that the thermoresponsive signal was progressively enhanced and the photosensitive signal gradually weakened by increasing the target concentration. Of note, the color of zone II transformed to blue (PB NPs) from white (blank) with the addition of the target since the released DNA−Fe_3O_4 NP conjugate could promote the formation of photothermal PB NPs in the presence of an acid and potassium ferrocyanide, and then the temperature signal increasingly heightened under NIR illumination (Scheme S1). As displayed in Figure 5a, there was an excellent linear proportional relationship between the thermoresponsive signal and the miRNA-141 concentrations ranging from 0.5 pM to 2 nM. The detection limit was calculated to be 0.29 pM (S/N = 3). Such performance demonstrates that the proposed photothermal sensing unit could achieve rapid analysis of the miRNA-141 with the help of handheld devices. Correspondingly, as depicted in Figures 5b and S6, the photocurrent signal varies inversely with the logarithm of the target concentration in the range of 0.001 pM to 5 nM with a detection limit of 0.43 fM (S/N = 3). In addition, the proposed foldable dual-signal sensing platform revealed comparable sensitivity by contrast with currently reported biosensors (Table S3).

Furthermore, given the complexity in real serum samples, herein, the interference of different base sequences was explored using 500 pM miRNA-155, miRNA-21, miRNA-429, single-base mismatched (Sm) miRNA-141, and the mixture as controls to prove the thermoresponsive-photoelectric sensing platform for miRNA-141 selectivity. It was obvious that the temperature signals produced in the sensing platform containing the interferent with the same concentration were apparently lower than that of miRNA-141 (Figure 5c). However, the photoelectric signals were the contrary, revealing no significant difference from the blank sample (Figure 5d). After blending the interferent (500 pM) with the target (50 pM), the intensity of temperature was soared and the PEC plummeted to the minimum. The excellent selectivity was attributed to the fact that the hairpin DNA retained the specific base complementary sequence for miRNA-141, indicating that the method based on thermoresponsiveness contained conspicuous anti-jamming characteristics. Simultaneously, the stability of the sensor was also a vital factor to be considered. The photocurrent responses in zone I were hardly changed through consecutive illumination, even after 1 month of storage, and the PATs in zone II still showed the same color as before (Figure S7), demonstrating the high stability of the thermoresponsive-photoelectric sensing platform for biological monitoring. To explore the practicality of the thermoresponsive-photoelectric sensing platform for real biological samples, the healthy human serum sample was implemented for miRNA-141 detection (details can be found in the Supporting Information and Tables S4 and S5).

CONCLUSIONS

In summary, an efficient lab-on-paper dual-signal platform was designed for microRNA-141 detection in body fluids, which introduced a versatile responsive unit with photothermal effects into the lab-on-paper PEC sensor. The instantaneous thermoresponsiveness for pre-judgement was based on exciton-transfer transition between Fe_3O_4 nanoparticles (Fe_3O_4 NPs) and PB NPs located on the photothermal unit driven by portable laser. Particularly, the visualized reference signal was directly presented as heat energy with the aid of a thermometer, thus preventing the deviation caused by identify gradients of color. Besides, the accurately quantified signal could be achieved by observing the photocurrent fluctuations, which was based on the antagonistic effect of Fe_3O_4 NPs on the $CuInS_2/CoIn_2S_4$ heterostructure in the photoelectric element. To integrate these superiorities, the multifunctional zone was parallelly coupled with the photoelectric unit to complete the linkage from semi-quantitative to precise analysis by fleet and precise transfer of the photothermal reagent with target-triggered properties on paper hydrophilic fluidic pathways. The steady, speedy, and maneuverable thermoresponsive-photoelectric sensing platform explored a new insight for POCT, and it was anticipated that this work had the potential for the early diagnosis of disease and the control of the epidemic. Furthermore, it is anticipated that the high affiliative and sensitive lab-on-paper will be developed for monitoring of trace metabolites by optimizing the configuration technology of the internal chip, extending more robust flexible substrate materials to combine with paper fibers, and growing photothermal−photoelectric materials with defects or polyphase crystal structures.

ASSOCIATED CONTENT

Supporting Information

The Supporting Information is available free of charge at https://pubs.acs.org/doi/10.1021/acssensors.2c01162.

Reagents and materials; apparatus; synthesis of the H2−Fe_3O_4 NPs conjugate; preparation of the Au NP functionalized working electrode; synthesis of $CoIn_2S_4$; synthesis of $CuInS_2$; optimization of the $CuInS_2/CoIn_2S_4$ heterojunction; optimization of the experimental conditions; and applications in real samples (PDF)

AUTHOR INFORMATION

Corresponding Authors

Li Li − *School of Chemistry and Chemical Engineering, University of Jinan, Jinan 250022, PR China;* orcid.org/0000-0003-2849-5984; Email: chm_lili@ujn.edu.cn

Jinghua Yu − *School of Chemistry and Chemical Engineering, University of Jinan, Jinan 250022, PR China;* orcid.org/0000-0001-5043-0322; Email: ujn.yujh@gmail.com

Yan Zhang − *School of Chemistry and Chemical Engineering, University of Jinan, Jinan 250022, PR China;* orcid.org/0000-0002-1936-4619; Email: chm_zhangyan@hotmail.com

Authors

Lin Li − *School of Chemistry and Chemical Engineering, University of Jinan, Jinan 250022, PR China*

Hongmei Yang − *School of Chemistry and Chemical Engineering, University of Jinan, Jinan 250022, PR China*

Xiaoran Tan − *School of Chemistry and Chemical Engineering, University of Jinan, Jinan 250022, PR China*

Shenguang Ge − *Institute for Advanced Interdisciplinary Research, University of Jinan, Jinan 250022, PR China;* orcid.org/0000-0002-0537-6491

https://doi.org/10.1021/acssensors.2c01162
ACS Sens. 2022, 7, 2429−2437

Lina Zhang − *Shandong Provincial Key Laboratory of Preparation and Measurement of Building Materials, University of Jinan, Jinan 250022, PR China*

Complete contact information is available at: https://pubs.acs.org/10.1021/acssensors.2c01162

Notes

The authors declare no competing financial interest.

■ ACKNOWLEDGMENTS

This work was financially supported by the National Natural Science Foundation of China (21874055 and 21904047), the Taishan Scholars Program, the Excellent Youth Innovation Team in Universities of Shandong (2021KJ021), and the Case-by-Case Project for Top Outstanding Talents of Jinan.

■ REFERENCES

(1) Colozza, N.; Tazzioli, S.; Sassolini, A.; Agosta, L.; di Monte, M. G.; Hermansson, K.; Arduini, F. Vertical-flow paper sensor for on-site and prompt evaluation of chloride contamination in concrete structures. *Anal. Chem.* **2021**, *93*, 14369−14374.

(2) Sun, F.; Ganguli, A.; Nguyen, J.; Brisbin, R.; Shanmugam, K.; Hirschberg, D. L.; Wheeler, M. B.; Bashir, R.; Nash, D. M.; Cunningham, B. T. Smartphone-based multiplex 30-minute nucleic acid test of live virus from nasal swab extract. *Lab Chip* **2020**, *20*, 1621−1627.

(3) Alafeef, M.; Dighe, K.; Moitra, P.; Pan, D. Rapid, ultrasensitive, and quantitative detection of SARS-CoV-2 using antisense oligonucleotides directed electrochemical biosensor chip. *ACS Nano* **2020**, *14*, 17028−17045.

(4) Hou, Y.; Lv, C. C.; Guo, Y. L.; Ma, X. H.; Liu, W.; Jin, Y.; Li, B. X.; Yang, M.; Yao, S. Y. Recent advances and applications in paper-based devices for point-of-care testing. *J. Anal. Test.* **2022**.

(5) Zhang, Y.; Xu, J.; Zhou, S.; Zhu, L.; Lv, X.; Zhang, J.; Zhang, L.; Zhu, P.; Yu, J. DNAzyme-triggered visual and ratiometric electrochemiluminescence dual-readout assay for Pb (II) based on an assembled paper device. *Anal. Chem.* **2020**, *92*, 3874−3881.

(6) Liu, Z.; Xiao, M.; Yang, R.; Zhou, Q.; Ye, H.; Yi, C. Multiplexed Detection of Fe^{3+}, Cobalamin and folate using fluorescent nanoprobe-based microarrays and a smartphone. *J. Anal. Test.* **2021**, *5*, 19−29.

(7) Zhu, L.; Lv, X.; Yu, H.; Tan, X.; Rong, Y.; Feng, W.; Zhang, L.; Yu, J.; Zhang, Y. Paper-based bipolar electrode electrochemiluminescence platform combined with pencil-drawing trace for the detection of M.SssI methyltransferase. *Anal. Chem.* **2022**, *94*, 8327−8334.

(8) Weiß, L. J. K.; Lubins, G.; Music, E.; Rinklin, P.; Banzet, M.; Peng, H.; Terkan, K.; Mayer, D.; Wolfrum, B. Single-impact electrochemistry in paper-based microfluidics. *ACS Sens.* **2022**, *7*, 884−892.

(9) Lee, H.; Lee, J.; Lee, S.-G.; Doyle, P. S. Hydrogel-based colorimetric assay for multiplexed microRNA detection in a microfluidic device. *Anal. Chem.* **2020**, *92*, 5750−5755.

(10) Suleman, S.; Shukla, S. K.; Malhotra, N.; Bukkitgar, S. D.; Shetti, N. P.; Pilloton, R.; Narang, J.; Nee Tan, Y.; Aminabhavi, T. M. Point of care detection of COVID-19: Advancement in biosensing and diagnostic methods. *Chem. Eng. J.* **2021**, *414*, 128759.

(11) Chen, C. Y.; Tan, Y. Z.; Hsieh, P. H.; Wang, C. M.; Shibata, H.; Maejima, K.; Wang, T. Y.; Hiruta, Y.; Citterio, D.; Liao, W. S. Metal-free colorimetric detection of pyrophosphate ions by inhibitive nanozymatic carbon dots. *ACS Sens.* **2020**, *5*, 1314−1324.

(12) Pu, Z. F.; Wu, B. C.; Tan, Y. H.; Wen, Q. L.; Ling, J.; Cao, Q. E. Selective aggregation of silver nanoprisms induced by monohydrogen phosphate and its application for colorimetric detection of chromium (III) Ions. *J. Anal. Test.* **2021**, *5*, 225−234.

(13) Gao, B.; Liu, H.; Gu, Z. An exothermic chip for point-of-care testing using a forehead thermometer as a readout. *Lab Chip* **2016**, *16*, 525−531.

(14) Chen, P.; Ma, Y.; Zheng, Z.; Wu, C.; Wang, Y.; Liang, G. Facile syntheses of conjugated polymers for photothermal tumour therapy. *Nat. Commun.* **2019**, *10*, 1192.

(15) Fu, G.; Zhu, Y.; Xu, K.; Wang, W.; Hou, R.; Li, X. Photothermal microfluidic sensing platform using near-infrared laser-driven multiplexed dual-mode visual quantitative readout. *Anal. Chem.* **2019**, *91*, 13290−13296.

(16) Zhou, W.; Fu, G.; Li, X. Detector-free photothermal bar-chart microfluidic chips (PT-chips) for visual quantitative detection of biomarkers. *Anal. Chem.* **2021**, *93*, 7754−7762.

(17) Zhou, W.; Hu, K.; Kwee, S.; Tang, L.; Wang, Z.; Xia, J.; Li, X. Gold nanoparticle aggregation-induced quantitative photothermal biosensing using a thermometer: A simple and universal biosensing platform. *Anal. Chem.* **2020**, *92*, 2739−2747.

(18) Fu, G.; Li, X.; Wang, W.; Hou, R. Multiplexed tri-mode visual outputs of immunoassay signals on a clip-magazine-assembled photothermal biosensing disk. *Biosens. Bioelectron.* **2020**, *170*, 112646.

(19) Yu, Z.; Gong, H.; Li, Y.; Xu, J.; Zhang, J.; Zeng, Y.; Liu, X.; Tang, D. Chemiluminescence-derived self-powered photoelectrochemical immunoassay for detecting a low-abundance disease-related protein. *Anal. Chem.* **2021**, *93*, 13389−13397.

(20) Li, L.; Zhang, Y.; Yan, Z.; Chen, M.; Zhang, L.; Zhao, P.; Yu, J. Ultrasensitive photoelectrochemical detection of microRNA on paper by combining a cascade nanozyme-engineered biocatalytic precipitation reaction and target-triggerable DNA motor. *ACS Sens.* **2020**, *5*, 1482−1490.

(21) Ulep, T.-H.; Zenhausern, R.; Gonzales, A.; Knoff, D. S.; Lengerke Diaz, P. A.; Castro, J. E.; Yoon, J.-Y. Smartphone based on-chip fluorescence imaging and capillary flow velocity measurement for detecting ROR^{1+} cancer cells from buffy coat blood samples on dual-layer paper microfluidic chip. *Biosens. Bioelectron.* **2020**, *153*, 112042.

(22) Cai, Q.; Yin, T.; Ye, Y.; Jie, G.; Zhou, H. Versatile photoelectrochemical biosensing for Hg^{2+} and aflatoxin B1 based on enhanced photocurrent of $AgInS_2$ quantum dot-DNA nanowires sensitizing NPC-ZnO nanopolyhedra. *Anal. Chem.* **2022**, *94*, 5814−5822.

(23) Liu, Q.; Shi, T.; Cheng, Y.; Wen, Z.; Ding, C.; Li, Y.; Wang, K. Amplified photocurrent signal for fabricating photoelectrochemical sulfadimethoxine aptasensor based on carbon nitride photosensitization with visible/near-infrared light responsive zinc phthalocyanine. *J. Hazard. Mater.* **2021**, *406*, 124749.

(24) Wu, Q.; Chu, M.; Shao, Y.; Wo, F.; Shi, D. Reduced graphene oxide conjugated with $CuInS_2$/ZnS nanocrystals with low toxicity for enhanced photothermal and photodynamic cancer therapies. *Carbon* **2016**, *108*, 21−37.

(25) Liu, J.; Zhao, X.; Xu, H.; Wang, Z.; Dai, Z. Amino acid-capped water-soluble near-infrared region $CuInS_2$/ZnS quantum dots for selective cadmium ion determination and multicolor cell imaging. *Anal. Chem.* **2019**, *91*, 8987−8993.

(26) Wang, Y.-q.; Rui, Y.-c.; Zhang, Q.-h.; Li, Y.-g.; Wang, H.-z. A facile in situ synthesis route for $CuInS_2$ quantum-dots/In_2S_3 Co-sensitized photoanodes with high photoelectric performance. *ACS Appl. Mater. Interfaces* **2013**, *5*, 11858−11864.

(27) Yuan, Y.-J.; Chen, D.-Q.; Huang, Y.-W.; Yu, Z.-T.; Zhong, J.-S.; Chen, T.-T.; Tu, W.-G.; Guan, Z.-J.; Cao, D.-P.; Zou, Z.-G. MoS_2 nanosheet-modified $CuInS_2$ photocatalyst for visible-light-driven hydrogen production from water. *ChemSusChem* **2016**, *9*, 1003−1009.

(28) Li, H.; Li, W.; Li, W.; Chen, M.; Snyders, R.; Bittencourt, C.; Yuan, Z. Engineering crystal phase of polytypic $CuInS_2$ nanosheets for enhanced photocatalytic and photoelectrochemical performance. *Nano Res.* **2020**, *13*, 583−590.

(29) Fu, G.; Wang, J.; Chen, Y.; Liu, Y.; Tang, Y.; Goodenough, J. B.; Lee, J.-M. Exploring indium-based ternary thiospinel as conceivable high-potential air-cathode for rechargeable Zn-Air batteries. *Adv. Energy Mater.* **2018**, *8*, 1802263.

(30) Hou, W.; Xiao, Y.; Han, G. An interconnected ternary $MIn_{(2)}S_{(4)}$ (M=Fe, Co, Ni) thiospinel nanosheet array: A type of efficient platinum-free counter electrode for dye-sensitized solar cells. *Angew. Chem., Int. Ed.* **2017**, *56*, 9146−9150.

(31) Xia, L.-Y.; Li, M.-J.; Wang, H.-J.; Yuan, R.; Chai, Y.-Q. Novel single-enzyme-assisted dual recycle amplification strategy for sensitive photoelectrochemical microRNA assay. *Anal. Chem.* **2020**, *92*, 14550−14557.
(32) Yang, H.; Hu, M.; Li, Z.; Zhao, P.; Xie, L.; Song, X.; Yu, J. Donor/acceptor-induced ratiometric photoelectrochemical paper analytical device with a hollow double-hydrophilic-walls channel for microRNA quantification. *Anal. Chem.* **2019**, *91*, 14577−14585.
(33) Kang, D.; Ahn, H. J.; Lee, J.; Kim, S. K.; Pyun, J.; Song, C.-S.; Kim, S. J.; Lee, J. An NIR dual-emitting/absorbing inorganic compact pair: A self-calibrating LRET system for homogeneous virus detection. *Biosens. Bioelectron.* **2021**, *190*, 113369.
(34) Lee, I.; Kim, S.-E.; Lee, J.; Woo, D. H.; Lee, S.; Pyo, H.; Song, C.-S.; Lee, J. A self-calibrating electrochemical aptasensing platform: Correcting external interference errors for the reliable and stable detection of avian influenza viruses. *Biosens. Bioelectron.* **2020**, *152*, 112010.
(35) Du, Y.; Li, X.; Lv, X.; Jia, Q. Highly sensitive and selective sensing of free bilirubin using metal-organic frameworks-based energy transfer process. *ACS Appl. Mater. Interfaces* **2017**, *9*, 30925−30932.
(36) Fu, G.; Sanjay, S. T.; Dou, M.; Li, X. Nanoparticle-mediated photothermal effect enables a new method for quantitative biochemical analysis using a thermometer. *Nanoscale* **2016**, *8*, 5422−5427.
(37) Lu, X.; Che, W.; Hu, X.; Wang, Y.; Zhang, A.; Deng, F.; Luo, S.; Dionysiou, D. D. The facile fabrication of novel visible-light-driven Z-scheme $CuInS_2/Bi_2WO_6$ heterojunction with intimate interface contact by in situ hydrothermal growth strategy for extraordinary photocatalytic performance. *Chem. Eng. J.* **2019**, *356*, 819−829.
(38) Liang, L.; Lan, F.; Yin, X.; Ge, S.; Yu, J.; Yan, M. Metal-enhanced fluorescence/visual bimodal platform for multiplexed ultrasensitive detection of microRNA with reusable paper analytical devices. *Biosens. Bioelectron.* **2017**, *95*, 181−188.
(39) Zhang, Y.; Li, Y. L.; Cui, S. H.; Wen, C. Y.; Li, P.; Yu, J. F.; Tang, S. M.; Zeng, J. B. Distance-based detection of Ag^+ with gold nanoparticles-coated microfluidic paper. *J. Anal. Test.* **2021**, *5*, 11−18.
(40) Zheng, J.; Liu, X.; Zhang, L. Design of porous double-shell $Cu_2O@CuCo_2O_4$ Z-Scheme hollow microspheres with superior redox property for synergistic photocatalytic degradation of multi-pollutants. *Chem. Eng. J.* **2020**, *389*, 124339.
(41) Hu, J.; Chen, C.; Zheng, Y.; Zhang, G.; Guo, C.; Li, C. M. Spatially separating redox centers on Z-Scheme $ZnIn_2S_4/BiVO_4$ hierarchical heterostructure for highly efficient photocatalytic hydrogen evolution. *Small* **2020**, *16*, 2002988.
(42) Nakada, A.; Nishioka, S.; Vequizo, J. J. M.; Muraoka, K.; Kanazawa, T.; Yamakata, A.; Nozawa, S.; Kumagai, H.; Adachi, S.-i.; Ishitani, O.; Maeda, K. Solar-driven Z-scheme water splitting using tantalum/nitrogen co-doped rutile titania nanorod as an oxygen evolution photocatalyst. *J. Mater. Chem. A* **2017**, *5*, 11710−11719.
(43) Cheng, Y.; Yang, F.; Xiang, G.; Zhang, K.; Cao, Y.; Wang, D.; Dong, H.; Zhang, X. Ultrathin tellurium oxide/ammonium tungsten bronze nanoribbon for multimodality imaging and second near-infrared region photothermal therapy. *Nano Lett.* **2019**, *19*, 1179−1189.

https://doi.org/10.1021/acssensors.2c01162
ACS Sens. 2022, 7, 2429−2437